DRAFT: IOWTC2020-3537

DRAFT: INVESTIGATION OF NONLINEAR DIFFERENCE-FREQUENCY WAVE EXCITATION ON A SEMISUBMERSIBLE OFFSHORE-WIND PLATFORM WITH BICHROMATIC-WAVE CFD SIMULATIONS

Lu Wang[1], Amy Robertson[1], Jason Jonkman[1], Yi-Hsiang Yu[1], Arjen Koop[2],
Adrià Borràs Nadal[3], Haoran Li[4], Wei Shi[5], Romain Pinguet[6],
Yang Zhou[7], Qing Xiao[7], Rupesh Kumar[8], Hamid Sarlak[9]

[1]National Renewable Energy Laboratory (NREL), Golden, CO
[2]Maritime Research Institute Netherlands (MARIN), Wageningen, Netherlands
[3]IFP Energies nouvelles (IFPEN), Rueil-Malmaison, France
[4]Norwegian University of Science and Technology (NTNU), Trondheim, Norway
[5]Dalian University of Technology (DUT), Dalian, China
[6]Principle Power, Inc. (PPI), Emeryville, CA
[7]University of Strathclyde (UOS), Glasgow, UK
[8]University of Ulsan (UOU), Ulsan, South Korea
[9]Technical University of Denmark (DTU), Kongens Lyngby, Denmark

ABSTRACT

The natural surge and pitch frequencies of semisubmersible offshore wind platforms are typically designed to be below the wave frequencies to avoid direct excitation. However, surge or pitch resonance can be excited by the nonlinear low-frequency loads generated by irregular incident waves. Traditional linear-wave potential-flow theory is unable to capture this phenomenon, while 2nd-order potential-flow models with added Morison drag were also found to consistently underpredict low-frequency excitation of the platform and the resulting motion response. As part of the new Offshore Code Comparison Collaboration, Continued, with Correlation and unCertainty (OC6) project under IEA Wind Task 30, Computational Fluid Dynamics (CFD) simulations were used to calculate the nonlinear loads on a fixed semisubmersible platform. The CFD results will hopefully enable a better understanding of the low-frequency loads in the future. Due to the high computing cost, CFD simulations of irregular waves can be challenging, especially if a full three-hour time window is to be covered. Instead, simulations were performed with bichromatic incident waves having a shorter repeat period, and the nonlinear difference-frequency loads were investigated. The primary focus of the current paper is to set up a computationally cost-effective CFD simulation for the load cases of interest and establish the corresponding uncertainty in the results. Preliminary comparison with Quadratic Transfer Functions from 2nd order potential-flow theory shows that CFD models consistently predict higher nonlinear wave loads at the difference frequency in the surge, heave, and pitch directions, likely due to flow separation and viscous drag not accounted for in potential-flow theory.

Keywords: semisubmersible, bichromatic waves, difference frequency, QTF, low frequency, 2nd order, wave load, computational fluid dynamics, CFD, IEA wind, OC6.

1. INTRODUCTION

As the support structure of a floating offshore-wind turbine, a semisubmersible platform has several advantages, which include the use of conventional mooring and possible quayside assembly and maintenance. Semisubmersibles are typically designed to have very low surge and pitch natural frequencies to avoid direct wave excitation. However, small nonlinear wave forces and moments at low frequencies can still induce large surge and pitch motion at the natural frequencies [1,2]. The low-frequency load and response of the platform are frequently under-predicted by current engineering modeling tools for floating offshore-wind systems, presenting a major obstacle to the accurate estimation of the ultimate and fatigue loads of floating wind systems.

The issue with under-predicting low-frequency wave excitation and platform response was identified in the previous Offshore Code Comparison Collaboration, Continued, with Correlation (OC5) project under Task 30 of the International Energy Agency (IEA) Wind [3]. Therefore, Phase I of the new OC6 (OC5 with unCertainty) project is dedicated to better understanding this issue and improving the predictions of the hydrodynamic load on, and the response of, a semisubmersible

platform at low frequencies. In the first part of OC6 Phase I, extensive investigations using simplified engineering models identified the inclusion of full Quadratic Transfer Functions (QTFs) from the second-order potential-flow theory as one of the model features that consistently improves the low-frequency predictions. In comparison, Newman's approximation was found to underestimate the second-order response in some cases [3,4]. Nevertheless, the global load and response near the surge and pitch resonance frequencies were still significantly underpredicted in irregular sea states with a full QTF [5,6]. Second-order potential-flow models augmented by Morison drag with a strip-theory formulation have also been evaluated. While a large drag coefficient was found to increase the low-frequency wave excitation on a fixed platform, the motion response under floating configuration became severely underpredicted [5,6].

To understand the reasons for the under-prediction of the low-frequency loads and responses in engineering-level tools, the OC6 project is setting up higher-fidelity simulations in Computational Fluid Dynamics (CFD) tools to investigate the phenomenon. The current paper presents the initial investigation of low-frequency loads using CFD tools, which forms the second part of OC6 Phase I. One major challenge associated with CFD is the long computing time needed to simulate the full three-hour time window typically required by irregular sea states. Therefore, the current CFD investigation instead focuses on bichromatic waves with short repeat periods, which significantly reduces the computing time, allowing more wave cases to be simulated for a more comprehensive understanding of the nonlinear low-frequency effects [7]. Furthermore, the difference-frequency loads obtained from the bichromatic-wave CFD simulations can be directly compared to potential-flow QTFs in order to identify the limitations of second-order potential-flow theory. Several previous studies also leveraged the convenience offered by bichromatic waves when investigating nonlinear wave loads and responses of offshore platforms and ships (see e.g. [4,8]). In this paper, a baseline set-up of the bichromatic-wave CFD simulation, including meshing and numerical settings, is documented along with convergence studies and uncertainty estimates. The baseline set-up was provided to each OC6 participants for reference. Using their own meshing tools and CFD software, each participant independently carried out the simulation for the same bichromatic-wave case with varying degrees of modification to the baseline set-up depending on the capabilities of the software used, the available computing resources, and past experience. The CFD results provided by the various OC6 participants were then gathered and compared with each other and to potential-flow predictions.

2. PROBLEM DESCRIPTION

A geometrically simplified version of the OC5-DeepCwind semisubmersible platform [3] was used in the current study. The platform consists of three identical columns, one upstream and two downstream, placed at the corners of an equilateral triangle. The center-to-center distance between each column is $L = 50$m. Each column has a radius of 6m and a draft of 14m. Below each column, a heave plate/base column of radius 12m and height 6m

is attached. Crossmembers (pontoons and braces) connecting the columns were all omitted, along with the central column.

The origin of the coordinate system is located on the free surface at the geometric center of the equilateral triangle. The $+x$-axis is in the direction of wave propogation, and the $+z$-axis points upward. Following the right-hand convention, the $+y$-axis points towards the starboard. The platform geometry and the adopted coordinate system are both shown in FIGURE 1.

The semisubmersible platform is fixed in space and subjected to the loads from bichromatic incident waves. The linear-wave (first-order) parameters for the two components of the incident waves are listed in TABLE 1. The mean water depth is 290m, and the deep-water limit applies to both primary wave components. The two wave components yield a difference frequency of $f_d = 0.032$Hz, which is approximately the pitch natural frequency of the OC5-DeepCwind semisubmersible. With linear-wave approximation, the bichromatic wave repeats itself every $T_R = 249.9$s.

All dimensional values presented in this paper are given at full scale; however, since we would eventually like to validate our CFD results against wave-tank measurements, the simulations were all carried out at 1:50 model scale instead, with the results scaled up based on Froude scaling during postprocessing.
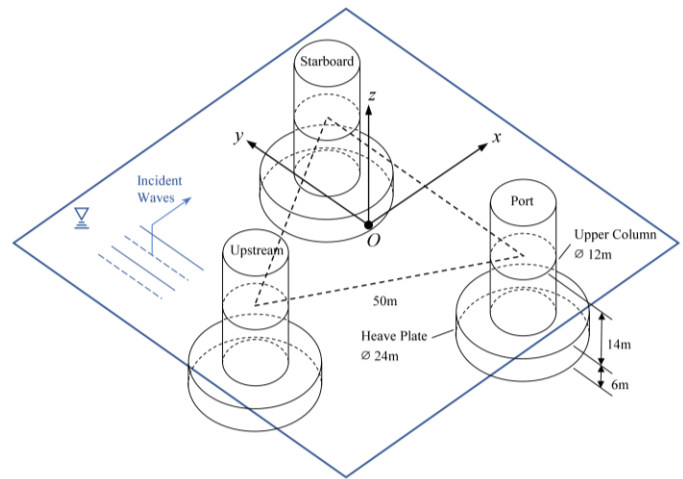
**FIGURE 1:** GEOMETRY OF THE SEMISUBMERSIBE PLATFORM AND THE ADOPTED COORDINATE SYSTEM.

TABLE 1: COMPONENTS OF BICHORMATIC INCIDENT WAVE

Wave	Period	Frequency	Wavelength	Amplitude
1	T_1=11.9s	f_1=0.084Hz	λ_1=221m	A_1=1.755m
2	T_2=8.6172s	f_2=0.116Hz	λ_2=116m	A_2=1.745m

3. NUMERICAL METHOD AND SET-UP

The Volume-of-Fluid (VOF) formulation was adopted by all CFD participants of the OC6 project. Both the air phase and the water phase are treated as viscous and incompressible fluids.

The boundary conditions used are largely consistent across all participants. Flow velocity and the free-surface level at the upstream boundary were prescribed based on the linear superposition of the velocity fields of the two wave components.
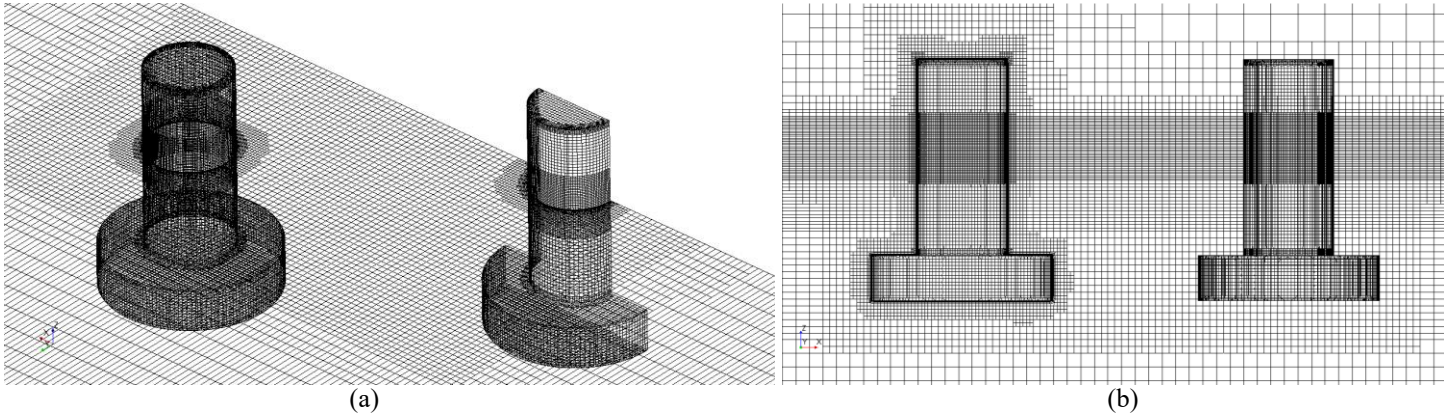
FIGURE 2: BASELINE MESH FOR THE BICHROMATIC-WAVE SIMULATION. (a) COLUMN SURFACE MESH AND WATERPLANE MESH. (b) COLUMN SURFACE MESH AND PLATFORM CENTER-PLANE MESH.

An upstream wave-forcing zone was also used by some participants to prevent wave reflection from the upstream boundary. A symmetry, free-slip, or no-slip condition was used on the two vertical side boundaries. If the simulation was performed on a half domain to exploit the port-starboard symmetry, the platform center plane was treated as a symmetry plane. The bottom was treated as either a no-slip or a free-slip surface. A wave-damping/relaxation zone typically at least $2\lambda_1$ long was placed next to the downstream boundary to minimize wave reflection. The downstream boundary was treated as a constant-dynamic pressure outlet or a zero-gradient boundary if a downstream wave-damping zone was used. Alternatively, the incident wave-field velocity can be prescribed on the downstream boundary to be consistent with a downstream wave-relaxation zone. Some participants also utilized non-reflecting boundary conditions (see Section 3.2). The top boundary was treated as a constant pressure inlet/outlet. A no-slip condition was enforced on the solid surface of the platform by all participants except IFP Energies nouvelles (see Section 3.2 for details).

Standard turbulence models led to excessive dissipation of the surface waves over time, resulting in a steady and continuous drop in wave-exciting forces. Therefore, all OC6 participants, except Technical University of Denmark (see Section 3.2), performed the simulation without any turbulence model.

3.1 Baseline Numerical Set-Up

To ensure a level of consistency in the quality of the numerical results across all participants, baseline domain size, grid resolution, time step, and numerical discretization schemes were specified. The exact set-up of each participant deviates from the baseline to varying degrees depending on the available computing resources and the capabilities of the software used.

The baseline numerical domain is 2004m long (approximately $9\lambda_1$), 100m wide from the platform center plane (2.7 times the maximum platform half width measured to the edge of the heave plate), and 390m tall. The upstream boundary is 442m ($2\lambda_1$) from the platform center ($x = 0$).

Since only a fixed platform was considered in the current work, dynamic mesh or overset grids were not required, and only a single fixed mesh was built. Nevertheless, for the sake of brevity, we shall describe the mesh as having two separate regions: a background wave mesh that encompasses the entire domain, and a platform mesh that covers the underwater region near the platform. A trimmed mesh with predominantly hexahedral cells was used outside the boundary-layer region. The grid sizes are given as multiples of the reference sizes h_w for the wave mesh and h_p for the submerged portion of the platform mesh. For the baseline case, we have $h_w = 0.45\text{m} \approx 2(A_1 + A_2)/15.5$ and $h_p = 0.9\text{m} \approx D/27$, where $D = 24\text{m}$ is the diameter of the heave plate.

To adequately resolve the bichromatic incident waves, the background wave mesh was refined near and right below the free surface. The regions of refinement, given by ranges of z-coordinates, and the corresponding grid sizes in the x-, y-, and z-directions, Δx, Δy, and Δz, are listed in TABLE 2. Away from the refinement regions, the mesh gradually transitioned to large isotropic cells $36h_w$ wide. There was no variation in grid size in the x- and y-directions except in the downstream damping zone where the mesh was suitably coarsened.

TABLE 2: REFINEMENT OF BACKGROUND WAVE MESH

z [m]	Δx	Δy	Δz
[-4, 4.5]	$2h_w$	$8h_w$	$0.5h_w$
[-10, -4]	$4h_w$	$8h_w$	$1h_w$
[-25, -10]	$4h_w$	$8h_w$	$2h_w$

Near the platform, the mesh was further refined to better resolve wave diffraction and flow separation from the platform. The regions of refinement and grid sizes for the platform mesh are listed in TABLE 3. To avoid spurious wave reflection, the grid sizes near the free surface in the x- and z-directions were kept consistent with the background wave mesh while Δy was reduced to be the same as Δx to better resolve the diffracted waves. Below the free surface, a uniform isotropic mesh was used to better capture any flow separation from the columns and the edges of the heave plates.

The surface of the platform was discretized into square patches with side $0.5h_p$, and a 10-layer boundary-layer mesh 0.4m thick was extruded from the surface. The thickness of each

layer increased linearly from the previous with the thinnest layer next to the solid surface being 1mm thick. The baseline mesh for a half domain, shown in FIGURE 2, consisted of 4.2M cells in total.

TABLE 3: REFINEMENT OF PLATFORM MESH

x [m]	y [m]	z [m]	Δx	Δy	Δz
[-47.5, 35]	[0, 45]	[-4, 4.5]	$2h_w$	$2h_w$	$0.5h_w$
[-45, 30]	[0, 40]	[-25, -4]	h_p	h_p	h_p

Second-order implicit time integration with a baseline time step of $\Delta t = T_2/1030$ was used. This choice of time step resulted in wave-based Courant numbers of 0.13 and 0.17 for the first and second wave components, respectively. All spatial discretization schemes were also formally second order. The numerical simulation was carried out for $2.5T_R$, equal to $52.5T_1$ or $72.5T_2$.

It should be noted that the adopted baseline grid size and time step likely do not yield fully converged results. However, the goal of the current work is not to simply present a fully converged solution for the single bichromatic-wave case considered. Rather, we would like to determine whether it is possible to perform such simulations for a host of similar cases under a reasonable amount of time with an acceptable level of uncertainty that renders the results useful for engineering design purposes. In Section 4, results from several repeated simulations with modified numerical configurations are presented to estimate the uncertainty associated with the above baseline set-up.

3.2 Numerical Set-Ups of OC6 Participants

In addition to the National Renewable Energy Laboratory (NREL), project participants from the Technical University of Denmark (DTU), the Dalian University of Technology (DUT), IFP Energies nouvelles (IFPEN), the Maritime Research Institute Netherlands (MARIN), the Norwegian University of Science and Technology (NTNU), Principle Power Inc. (PPI), the University of Strathclyde (UOS), and the University of Ulsan (UOU) have all provided simulation results for the load case in question.

NREL results were obtained with the commercial CFD software STAR-CCM+ ver. 13.06.012 [9]. Due to port-starboard symmetry, the simulation was carried out with only the starboard half of the platform. The baseline set-up described in Section 3.1 was adopted without modification. No upstream wave-relaxation zone was utilized, while a wave-damping zone $2\lambda_1$ long was placed next to the downstream boundary. For each time step, 20 inner iterations were used. The residuals were observed to rapidly decrease first and subsequently level off to a minimum value within the 20 iterations in NREL simulations.

IFPEN performed the simulation using OpenFOAM ver. 1812 [10] with the waves2Foam toolbox [11]. A full-domain mesh instead of half was built for the simulation. However, the computational mesh lacked an extruded region for the boundary layer. The boundary condition on the platform surface was also changed to free slip. Since we expect viscous effects to manifest primarily through flow separation from the sharp corners of the heave plates, we anticipate the effect of not resolving the boundary layer on the global forces and moments to be limited. Wave-forcing/relaxation zones $1.0\lambda_1$ and $2.0\lambda_1$ long were used upstream and downstream, respectively.

DTU performed the simulation using the IHFOAM solver [12] with OpenFOAM ver. 1812 [10] on the full-domain mesh built by IFPEN. The simulation also utilized a newly developed less-dissipative stabilized RANS solver (stabRAS) based on the k-ω SST model [13]. Finally, instead of a downstream wave relaxation/damping zone, an active absorption boundary condition based on the shallow water assumption was imposed on the downstream boundary [14].

DUT also carried out the simulation using STAR-CCM+ ver. 13.06.012 [9] on a half domain. The domain size, grid resolution, and time step all follow the baseline set-up with 5 inner iterations per time step.

MARIN generated a half-domain mesh using HEXPRESS [15] following the grid-size and domain-size guidelines provided in Section 3.1. The simulation was performed using ReFRESCO [16] according to the baseline set-up. During each time step, 100 inner iterations were used to minimize error build-up over time. Upstream and downstream wave-relaxation zones $1.5\lambda_1$ and $3.0\lambda_1$ long, respectively, were employed. Furthermore, non-reflective Sommerfeld-type boundary conditions were applied on the inlet and outlet to minimize reflections of the long difference-frequency free waves (see Section 4.1).

NTNU performed the simulation with OpenFOAM ver. 1712 [17] and waves2Foam [11]. The baseline set-up was adopted except that the grid size in the y-direction, Δy, on the free surface (first mesh refinement region in TABLE 2) was halved. Wave-forcing/relaxation zones $1.0\lambda_1$ and $4.0\lambda_1$ long were used upstream and downstream, respectively.

PPI also carried out the simulation using OpenFOAM ver. 1812 [10] and waves2Foam [11]. The full-domain mesh built by IFPEN was used. Wave-relaxation zones $1.5\lambda_1$ and $2.0\lambda_1$ long were placed next to the upstream and downstream boundaries, respectively.

UOS simulated the problem using OpenFOAM ver. 4.x [18] with waves2Foam [11]. The same full-domain mesh built by IFPEN was used. Wave-relaxation zones $1.5\lambda_1$ and $4.0\lambda_1$ long were placed next to the upstream and downstream boundaries, respectively. A much finer time step of $\Delta t = T_2/2438$ was adopted. All other settings were consistent with the baseline.

UOU performed the simulation with ANSYS Fluent ver. 19.2 [19]. The baseline (half-domain) mesh was used without modification. A slightly larger time step of $\Delta t = T_2/862$ was adopted with 35 inner iterations per time step. The downstream wave-damping zone is $2.0\lambda_1$ long.

4. ANALYSIS AND PROCESSING OF NUMERICAL RESULTS

To ascertain the quality of the generated waves, the bichromatic incident waves were simulated first in 2D without the platform present. Subsequently, simulations with the fixed platform were carried out to obtain the wave loads on the platform. Furthermore, NREL has carried out a convergence study by repeating the simulation several times with different time steps,

grid sizes, and domain widths in order to estimate the uncertainty in the obtained wave loads, both at the wave frequencies and at the difference frequency. Due to the number of simulations needed and the computing resources required, the systematic numerical uncertainty analysis was performed for the NREL results only. In this section, this uncertainty estimation is presented. The results from all OC6 participants are compared to each other in Section 5 as well as to second-order potential-flow results.

4.1 Bichromatic Incident Waves

The bichromatic incident waves were first simulated without the presence of the platform. A two-dimensional mesh with a resolution in the xz-plane equivalent to the baseline mesh described in Section 3 was used for the wave-only simulations. The wave-elevation time series at various x-positions along the domain were recorded, and Fast Fourier Transform (FFT) were performed on the time series from the last available repeat period $t \in [1.5T_R, 2.5T_R)$ to obtain the amplitudes at the wave frequencies and the difference frequency. The wave amplitudes at the upstream boundary were calibrated to obtain the target wave amplitudes given in TABLE 1, to within 0.5% difference by NREL, at $x = 0$ with the baseline grid size and time step. All OC6 project participants independently went through the same wave calibration process to ensure consistent incident waves.

To investigate grid convergence, a fine and a coarse mesh were constructed by halving and doubling the reference grid size h_w while maintaining the ratios shown in TABLE 2. Temporal convergence was investigated by simulating the waves on the baseline mesh using either half or double the baseline time step. The inlet wave amplitudes calibrated for the baseline grid and time step were consistently used in all runs of the convergence study.

The wave amplitudes at the two wave frequencies measured at $x = 0$ (the platform center location) are listed in TABLE 4. Overall, the wave amplitudes show weak dependence on time step but stronger dependence on grid size for the range of time step and grid size considered. Nevertheless, the level of convergence for the wave-only case was considered adequate with the baseline grid size of $h_w = 0.45$m and time step of $\Delta t = T_2/1030$; further reducing the time step or grid size did not significantly change the wave amplitudes.

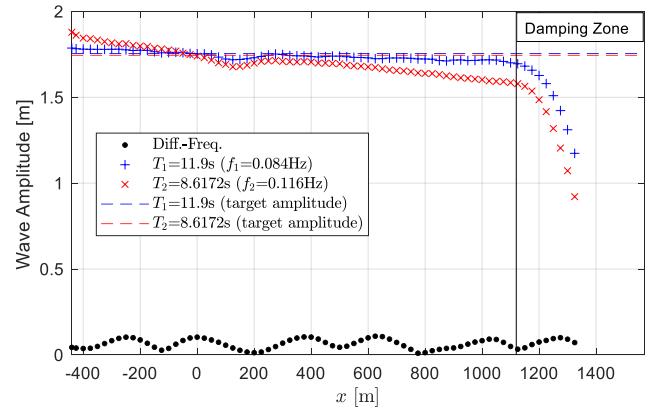### TABLE 4: WAVE AMPLITUDES AT $x = 0$.

Wave	$h_w = 0.45$m $\Delta t = T_2/515$	$h_w = 0.45$m $\Delta t = T_2/1030$	$h_w = 0.45$m $\Delta t = T_2/2060$
1	$A_1 = 1.745$m	$A_1 = 1.754$m	$A_1 = 1.755$m
2	$A_2 = 1.736$m	$A_2 = 1.740$m	$A_2 = 1.740$m
Wave	$h_w = 0.9$m $\Delta t = T_2/1030$	$h_w = 0.45$m $\Delta t = T_2/1030$	$h_w = 0.225$m $\Delta t = T_2/1030$
1	$A_1 = 1.931$m	$A_1 = 1.754$m	$A_1 = 1.758$m
2	$A_2 = 1.663$m	$A_2 = 1.740$m	$A_2 = 1.779$m

The wave amplitudes obtained with the baseline grid and time step at various x-positions are presented in FIGURE 3. Outside the damping zone, the amplitude of the low-frequency (f_1=0.084Hz) wave component remains relatively constant over the entire domain. Meanwhile, some wave dissipation can be

observed for the high-frequency (f_2=0.116Hz) wave component. The slight decrease in wave amplitude downstream was compensated by calibrating the inlet wave amplitudes as discussed previously.

The wave amplitude at the difference frequency (f_d) varies with x. Upon closer inspection, the modulation of the diff.-freq. amplitude was found to be the result of the superposition of three different wave components at the difference frequency: incident bound waves, incident free waves, and reflected free waves from the downstream boundary. The incident bound waves come from the nonlinear interactions between the two primary wave components. The bound waves do not satisfy the linear dispersion relation and have wavenumber $k_b = |k_1 - k_2|$ where k_1 and k_2 are the wavenumbers of the two primary waves. The incident free waves, on the other hand, were likely generated by imperfect wave making at the upstream boundary. While nonlinear in origin, the free waves satisfy the linear-wave dispersion relation. The low frequency of the free waves leads to a very long wavelength of λ_d =1336m, which is comparable to the domain length and significantly longer than the downstream damping zone. As a result, the incident free waves cannot be effectively absorbed, resulting in reflected free waves. Strictly speaking, there should also be reflected bound waves. However, since the two primary wave components were effectively absorbed by the damping zone, the reflected bound waves were negligible.

FIGURE 3: WAVE AMPLITUDES AT VARIOUS x-POSITIONS OBTAINED WITH THE BASELINE GRID AND TIME STEP

By adapting the wave splitting method from [20], we can reliably decompose the three wave components at the difference frequency. The complex wave amplitudes, $A_{d1}, A_{d2}, \dots, A_{dn}$, at the difference frequency at n different x-positions, $x_1, x_2, \dots, x_n$ can be assumed to have the form

$$A_{dj} = \zeta_{if} e^{-ik_d x_j} + \zeta_{rf} e^{ik_d x_j} + \zeta_{ib} e^{-ik_b x_j}, \ j = 1,2,\dots,n \quad (1)$$

where i $= \sqrt{-1}$ and ζ_{if}, ζ_{rf}, and ζ_{ib} are the constant and complex amplitudes of the incident free waves, reflected free waves, and the incident bound waves, respectively. The wavenumber of the difference-frequency free waves, k_d, can be determined from the linear-wave dispersion relation. If A_{dj} is known at $n \geq 3$

different x-positions, as in FIGURE 3, a linear system of equations can be formed to solve for ζ_{if}, ζ_{rf}, and ζ_{ib}:

$$\begin{bmatrix} e^{-ik_dx_1} & e^{ik_dx_1} & e^{-ik_bx_1} \\ \vdots & \vdots & \vdots \\ e^{-ik_dx_n} & e^{ik_dx_n} & e^{-ik_bx_n} \end{bmatrix}\begin{bmatrix} \zeta_{if} \\ \zeta_{rf} \\ \zeta_{ib} \end{bmatrix} = \begin{bmatrix} A_{d1} \\ \vdots \\ A_{dn} \end{bmatrix}, \qquad (2)$$

assuming the choices of x_j do not result in a singular system. A minimum of $n = 3$ is needed to solve Eq. (2); however, it is more reliable to have $n \gg 3$ and solve Eq. (2) in the least-square sense. In this paper, the wave amplitudes at 28 different x-positions equally spaced between $x = -275$m to 400m were used to decompose the difference-frequency waves. The results were not sensitive to the choices of x-positions so long as they were not too close to the upstream boundary or the downstream damping zone. For the waves shown in FIGURE 3, we have $|\zeta_{if}| =$ 0.0515m, $|\zeta_{rf}| = 0.0190$m, and $|\zeta_{ib}| = 0.0418$m. The value of $|\zeta_{ib}|$ is in good agreement with the theoretical value given by the 2nd-order potential-flow theory $A_1A_2|k_1 - k_2|/2 = 0.0395$m [21]. This agreement was consistently observed for several different bichromatic-wave cases we have tested. It is especially remarkable considering that the smallest grid size in the z-direction on the free surface is 0.225m, larger than the difference-frequency wave amplitude. It appears that we were able to extract subgrid-scale information using the wave-elevation time series measured at multiple points in the domain.

The amplitude of the free waves at the difference frequency were found to be sensitive to the overall domain length. With the baseline numerical set-up, i.e. upstream velocity inlet with downstream wave-damping zone, we have observed resonance behavior of the difference-frequency free waves when the overall domain length is an odd multiple of a quarter of the wavelength λ_d. Since we are interested in obtaining results for pure bichromatic waves, resonance should be avoided to minimize the impact of the free waves on the difference-frequency wave loads. Therefore, an overall domain length of 2004m= $6/4\lambda_d$ was used.

4.2 Wave Excitation on Fixed Platform

With the quality of the bichromatic incident waves evaluated, 3D simulations were performed with the semisubmersible platform in waves. The wave-induced surge force, F_x, heave force, F_z, and pitch moment, M_y, on the fixed semisubmersible platform were evaluated from the CFD results. The quantities of interest are the difference-frequency amplitudes of F_x and M_y and, to a much lesser degree, that of F_z. The wave-frequency amplitudes of the wave excitation are also presented for completeness. The load amplitudes were obtained by performing an FFT on a section of the force/moment time series from a time window T_R wide. The FFT of the surge force computed from the time window $t \in [1.5T_R, 2.5T_R)$ is shown in FIGURE 4.

In the rest of the paper, all amplitudes of wave-exciting forces and moments are normalized by the factors listed in TABLE 5 where ρ, g, L, and A_{wp} are the water density,

gravitational acceleration, center-to-center distance between columns, and the waterplane area of the platform, respectively.

The obtained force/moment amplitudes fluctuate slightly depending on the time window used for the FFT analysis. To investigate the level of variation, the force amplitude was calculated from the FFT of the force time series over a sliding time window $t \in [t_s, t_s + T_R)$ where t_s is the start of the window. FIGURE 5 shows how the difference-frequency amplitude of F_x changes with the sliding window. Initial transient behavior is observed up to $t_s/T_R = 0.5$, after which the normalized force amplitude starts to fluctuate about a mean value of 0.84. To avoid the initial transient phase, we consistently used the last available time window $t \in [1.5T_R, 2.5T_R)$ to compute the force/moment amplitudes in all subsequent analysis.
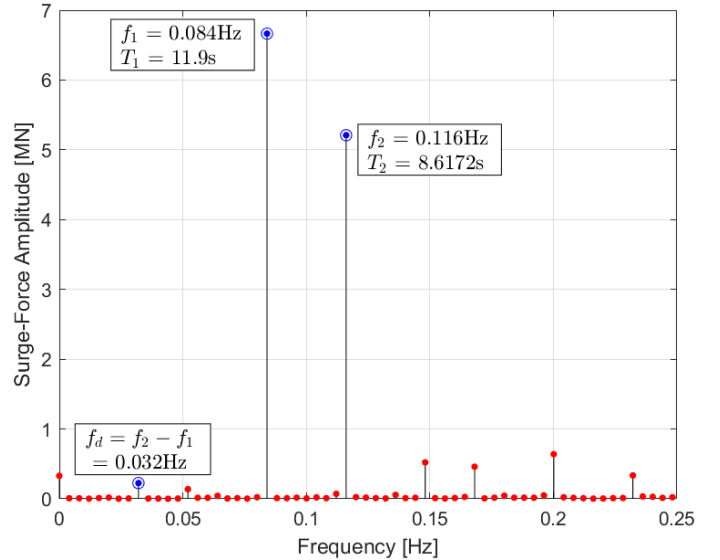

FIGURE 4: AMPLITUDE OF SURGE FORCE OBTAINED BY PERFORMING FFT OVER $t \in [1.5T_R, 2.5T_R)$ WITH FREQUENCY COMPONENTS OF INTEREST LABELED.
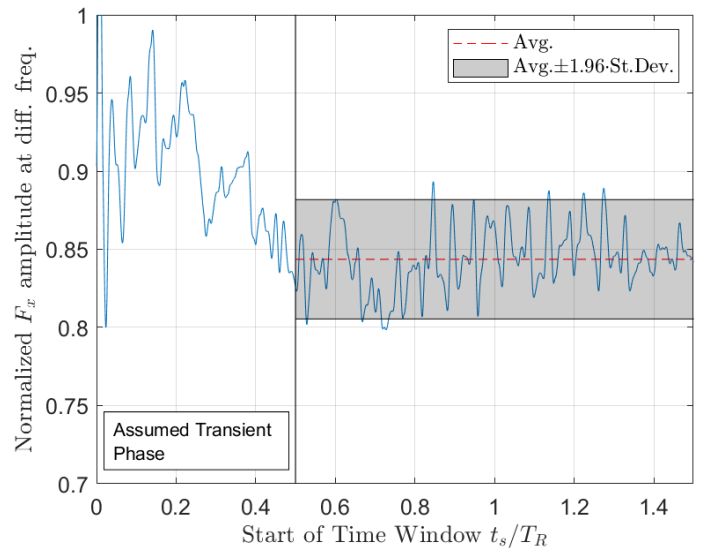

FIGURE 5: VARIATION OF SURGE-FORCE AMPLITUDE AT THE DIFFERENCE FREQUENCY WITH TIME WINDOW.

TABLE 5: NORMALIZATION FACTORS FOR FORCE/MOMENT AMPLITUDES

	Diff.-Freq. (f_d)	1st Wave Freq. (f_1)	2nd Wave Freq. (f_2)
F_x	$\rho g A_{wp} A_1 A_2 (k_1 - k_2)$	$2\rho g A_{wp} A_1$	$2\rho g A_{wp} A_2$
F_z	$0.5\rho g A_{wp} A_1 A_2 (k_1 - k_2)$	$\rho g A_{wp} A_1$	$\rho g A_{wp} A_2$
M_y	$0.5\rho g L A_{wp} A_1 A_2 (k_1 - k_2)$	$\rho g L A_{wp} A_1$	$\rho g L A_{wp} A_2$

All force/moment amplitudes computed using the baseline numerical configuration and the final time window of $t \in [1.5T_R, 2.5T_R)$ are listed in TABLE 6.

TABLE 6: NORMALIZED WAVE-LOAD AMPLITUDES COMPUTED USING THE BASELINE CONFIGURATION

	Diff. Freq. (f_d)	1st Wave Freq. (f_1)	2nd Wave Freq. (f_2)
F_x	0.8408	0.5570	0.4387
F_z	1.7662	0.4420	0.4231
M_y	1.6815	0.3929	0.4427

4.2.1 Uncertainty in Wave Forces and Moments

One major objective of the current work is to estimate the uncertainties in the wave-exciting forces and moments predicted by CFD, especially in the wave loads at the difference frequency. While there are potentially many sources of errors and uncertainties, the following three were considered to be the major ones: numerical uncertainty dominated by temporal and spatial discretization error (U_1), modeling uncertainty due to the finite numerical domain size (U_2), and, finally, processing uncertainty associated with the minor fluctuation of force/moment amplitudes over analysis time (U_3) as demonstrated in FIGURE 5. The three sources of uncertainty are distinct in nature and were assumed independent. Therefore, the total uncertainty can be estimated as $U_{tot} = (\sum_{i=1}^{3} U_i^2)^{1/2}$.

Numerical uncertainty from discretization error

Temporal and spatial convergence can be evaluated together by maintaining an appropriate ratio between time step and grid size during mesh refinement and coarsening. However, for more flexibility, we opted to perform separate investigations on the effect of time step and grid size. To estimate the temporal discretization error, the simulation was repeated with the baseline mesh using four increasingly finer time steps. The finest temporal resolution was achieved using an adaptive-time step solver to limit the convective Courant number to below 0.5. The resulting mean time step was approximately $\overline{\Delta t} = T_2/5390$. With the exception of the surge-force amplitude at the higher second wave frequency (f_2), monotonic convergence with time step was observed for all quantities listed in TABLE 6. As an example, the pitch-moment amplitudes at the difference and wave frequencies are shown in FIGURE 6 for the four different time steps considered. The normalized difference-frequency amplitudes are scaled by a factor of 0.1 to fit better with the wave-frequency amplitudes in the same plot. For reference, the predictions from linear potential-flow (Lin. Pot.) theory are also included for the two primary wave frequencies.

To fully exploit the observed monotonic convergence, the uncertainty associated with temporal discretization was estimated using the method based on Richardson extrapolation

[22]. The standard power-law error estimator was adopted for the discretization error:

$$\phi_i - (\phi_0 + e_0) = \delta_{RE} = \alpha_t (\Delta t)_i^{p_t} \tag{3}$$

where ϕ_i is a scalar quantity of interest obtained using the ith choice of time step. The exact value of the same quantity obtained at the limit of infinite temporal and spatial resolution is given by ϕ_o. The constant e_0 represents the spatial discretization error associated with the baseline grid. The three constants ($\phi_0 + e_0$), α_t, and p_t are determined using the available results obtained with different time steps. More specifically, the constants were chosen to minimize the function:

$$S(\phi_0 + e_0, \alpha_t, p_t) = \sqrt{\sum_{i=1}^{n_t} \left[\phi_i - (\phi_0 + e_0 + \alpha_t (\Delta t)_i^{p_t})\right]^2} \tag{4}$$

where $n_t = 4$ is the number of different time steps used. Following the recommendation given in [22], the uncertainty due to temporal discretization was estimated as:

$$U_{\Delta t} = \begin{cases} \min(1.25|\delta_{RE}| + U_s, 1.25\Delta_M) & \text{for } 0 < p_t \leq 0.95 \\ 1.25|\delta_{RE}| + U_s & \text{for } 0.95 < p_t < 2.05 \\ \max(1.25|\delta_{RE}^*| + U_s, 1.25\Delta_M) & \text{for } p_t \geq 2.05 \end{cases} \tag{5}$$

where U_s is the standard deviation of the least-squares fit [23]:

$$U_s = \sqrt{\frac{\sum_{i=1}^{n_t}\left[\phi_i - (\phi_0 + e_0 + \alpha_t (\Delta t)_i^{p_t})\right]^2}{n_t - 3}}. \tag{6}$$

The error estimate δ_{RE}^* is obtained by setting the order of convergence p_t to the theoretical value of 2. The data range Δ_M is the maximum difference in ϕ_i across all available simulations:

$$\Delta_M = \max(|\phi_i - \phi_j|) \text{ for } 1 \leq i, j \leq n_t. \tag{7}$$

If the convergence is not monotonic, the range-based estimate for uncertainty is used [22,24]:

$$U_{\Delta t} = 3\Delta_M \tag{8}$$

which is approximately consistent with a 95% confidence interval [24].
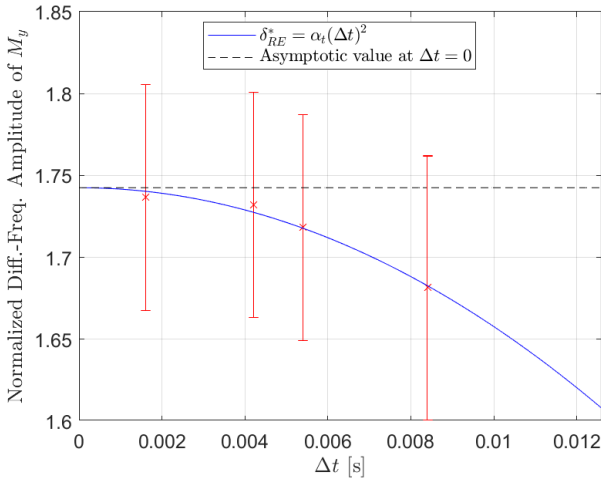
The Richardson extrapolation for the normalized pitch-moment at the difference frequency is shown in FIGURE 7. The CFD results obtained with the four different time steps are shown as red crosses along with the uncertainty intervals estimated using Eq. (5). Monotonic convergence with time step is observed. However, the order of convergence p_t obtained by minimizing the function in Eq. (4) is greater than 2.05. Therefore, the extrapolation was performed instead with $p_t = 2$ to obtain δ_{RE}^*. The estimated $U_{\Delta t}$ of the baseline solution ($\Delta t = T_2/1030$) for all quantities of interest are listed in TABLE 7.

The spatial discretization error was investigated by repeating the simulation with two increasingly finer platform meshes and the baseline time step of $\Delta t = T_2/1030$. The finer (6.2M cells) and the finest (12.3M cells) grids were constructed by halving and quartering the reference size h_p (see TABLE 3) from the baseline value. The cell thickness in the boundary layer

mesh was also halved and quartered. The size of the platform surface mesh was maintained at $0.5h_p$ for the baseline and finer grids; however, h_p was used for the finest mesh to avoid an excessive number of cells. It should be noted that the background wave mesh and the free-surface mesh near the platform were kept the same for all cases with $h_w = 0.45$m since the convergence of the wave mesh was already investigated in Section 4.1. Furthermore, the slight wave dissipation caused by finite grid resolution was already accounted for during wave calibration. Keeping the same background wave mesh has the benefit of maintaining consistent incident waves at the location of the platform, allowing us to focus on the convergence of the nearfield flow.
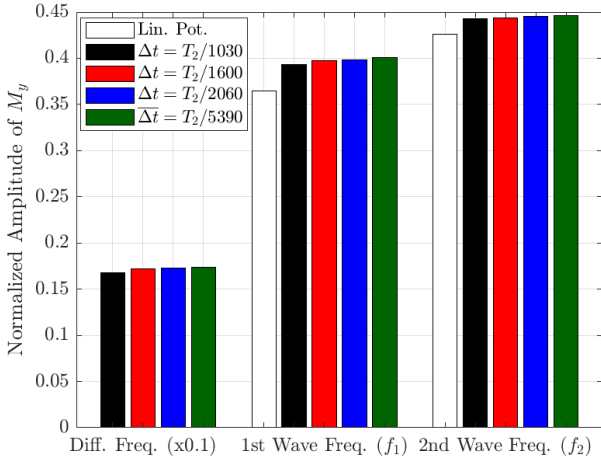
FIGURE 6: NORMALIZED PITCH-MOMENT AMPLITUDE AT THE DIFFERENCE FREQUENCY AND THE TWO WAVE FREQUENCIES OBTAINED WITH DIFFERENT TIME STEPS.
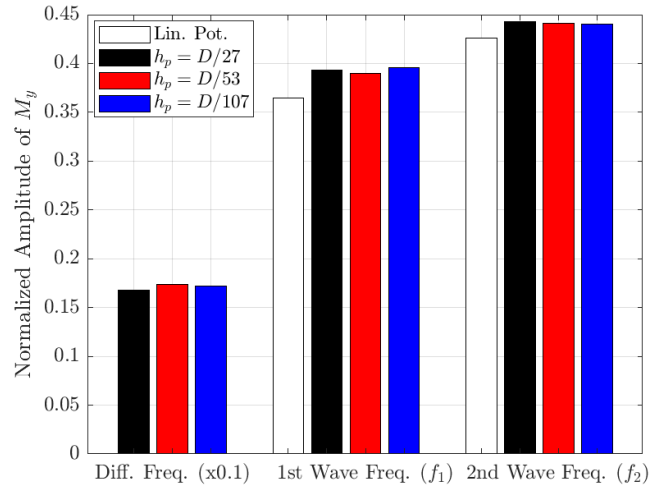

FIGURE 7: RICHARDSON EXTRAPOLATION WITH TIME STEP FOR THE NORMALIZED PITCH-MOMENT AMPLITUDE AT THE DIFFERENCE FREQUENCY.

TABLE 7: TEMPORAL-DISCRETIZATION UNCERTAINTIES IN WAVE-LOAD AMPLITUDES FOR THE BASELINE SOLUTION

	Diff. Freq. (f_d)	1st Wave Freq. (f_1)	2nd Wave Freq. (f_2)
F_x	±5.5%	±0.7%	±3.8%
F_z	±13%	±3.3%	±5.0%
M_y	±4.9%	±2.7%	±1.1%

As an example, FIGURE 8 shows the amplitudes of the wave pitch moment computed with the three different grid resolutions. The characteristic grid size near the platform, h_p, is expressed as a fraction of the heave-plate diameter $D = 24$m. Overall, the change in pitch-moment amplitudes with grid size is small. However, the convergence with grid size is non-monotonic, likely because the mesh resolution is not fully in the asymptotic regime and the three grids are not completely geometrically similar. Similar observations were also made for surge and heave forces.

The lack of apparent asymptotic convergence renders the estimation of spatial discretization uncertainty more difficult. Mathematically rigorous approaches based on Richardson extrapolation [22] cannot be reliably applied. Instead, we resorted to the range-based estimation for all spatial discretization uncertainties, i.e. $U_{\Delta x} = 3\Delta_M$ where Δ_M is the maximum difference in a quantity of interest among the results from all three grids. The large safety factor of 3 reflects the fact that the error estimated based on Δ_M is not as reliable [23]. Indeed, the reliability of the above estimation strongly depends on the available results; Δ_M can be made artificially small if only very similar grid sizes are considered. In the present work, however, we have covered significant changes in grid size in the convergence study; therefore, the range-based estimate should yield an uncertainty estimate that is meaningful. The uncertainty from spatial discretization is listed in TABLE 8. Generally, $U_{\Delta x}$ is comparable to $U_{\Delta t}$ for the wave-frequency loads but is significantly higher for those at the difference frequencies, especially for the heave force. The larger uncertainty reflects the challenges in capturing the small difference-frequency loads with numerical simulations.

FIGURE 8: NORMALIZED PITCH-MOMENT AMPLITUDE AT THE DIFFERENCE FREQUENCY AND THE TWO WAVE FREQUENCIES OBTAINED WITH DIFFERENT GRID SIZES.

TABLE 8: SPATIAL-DISCRETIZATION UNCERTAINTIES IN WAVE-LOAD AMPLITUDES FOR THE BASELINE SOLUTION

	Diff. Freq. (f_d)	1st Wave Freq. (f_1)	2nd Wave Freq. (f_2)
F_x	±18%	±2.3%	±1.4%
F_z	±32%	±5.2%	±5.5%
M_y	±9.7%	±4.3%	±1.7%

To obtain the total discretization uncertainty U_1, the estimated temporal and spatial uncertainties listed in TABLE 7 and TABLE 8 were conservatively combined through direct summation.

Modeling uncertainty due to the finite domain width

The uncertainty caused by the finite domain size was primarily controlled by the domain width since the side boundaries were much closer to the platform than the upstream and downstream boundaries. Of course, as discussed in Section 4.1, the overall domain length may affect the difference-frequency free waves that can impact the second-order wave loads. However, it is possible to effectively minimize and subsequently remove the contribution from the free waves by first choosing an appropriate overall domain length and applying the correction procedure described in Section 4.2.2.

The effect of domain width was investigated by repeating the simulation with progressively higher $w_{1/2}$, the width of the half domain measured from the platform center plane to the starboard boundary. Four different domain widths from the baseline case of $2w_{1/2}/L = 4$ up to the widest domain of $2w_{1/2}/L = 20$ were considered. The amplitudes of surge force are shown in FIGURE 9. For the first and second wave frequencies, the predictions from linear potential-flow (Lin. Pot.) theory are also included for reference. Overall, the predicted force amplitudes are similar across the different cases except for the intermediate domain width of $2w_{1/2}/L = 6$. A significant increase in surge force at the second wave frequency and the difference frequency can be observed. Heave force and pitch moment also showed similar behaviors. This was likely caused by the resonance of the diffracted waves at the second wave frequency. The exact resonance mechanism requires further investigation. The results in FIGURE 9 demonstrate the importance of investigating domain-width effects in numerical wave-tank simulations. The convergence of the results with increasing domain width may not be monotonic due to potential wave resonance, and an improperly chosen domain width may lead to large modeling errors.
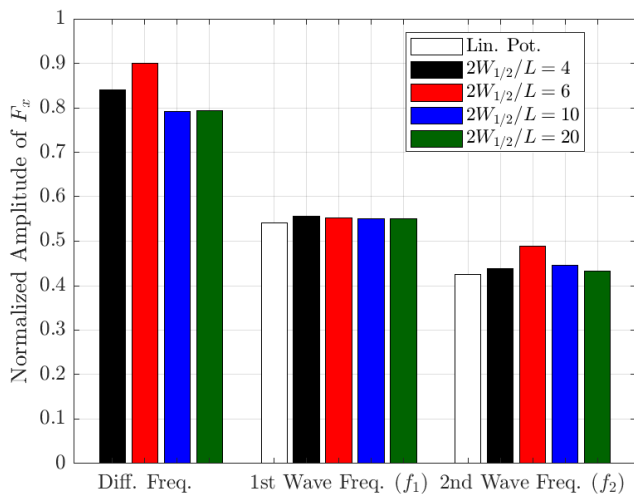

FIGURE 9: EFFECT OF NUMERICAL DOMAIN WIDTH ON THE NORMALIZED AMPLITUDES OF SURGE FORCE.

The differences between the results of the baseline set-up ($2w_{1/2}/L = 4$) and those of the widest domain ($2w_{1/2}/L = 20$) were multiplied by a safety factor of 2 to provide an estimate of the modeling uncertainty for the baseline solution. The resulting estimates are listed in TABLE 9 as percentages of the baseline solution listed in TABLE 6.

TABLE 9: UNCERTAINTIES IN WAVE-LOAD AMPLITUDES DUE TO FINITE DOMAIN WIDTH

	Diff. Freq. (f_d)	1st Wave Freq. (f_1)	2nd Wave Freq. (f_2)
F_x	±12%	±2.6%	±2.9%
F_z	±1.8%	±5.8%	±6.2%
M_y	±7.8%	±3.0%	±1.0%

Processing uncertainty from the fluctuation in load amplitudes

The uncertainty associated with the fluctuation in force/moment amplitudes over processing time illustrated in FIGURE 5 can be accounted for by introducing an additional uncertainty U_3. For the sake of consistency among participants, the results from the very last time window, i.e. the values with $t_s = 1.5T_R$, were taken as the final results instead of the mean values (the red dashed line in FIGURE 5). Therefore, we simply have $U_3 = 2\sigma$ where σ is the standard deviation of the fluctuation about the mean. The $\pm 2\sigma$ interval about the mean is shown as a grey band in FIGURE 5. The values of U_3 expressed as percentages of the baseline solution are listed in TABLE 10. Relatively large fluctuation is observed for the difference-frequency heave force. The wave loads at the two wave frequencies all show negligible fluctuation over time.

TABLE 10: UNCERTAINTIES IN WAVE-LOAD AMPLITUDES DUE TO FLUCTUATION OVER TIME

	Diff. Freq. (f_d)	1st Wave Freq. (f_1)	2nd Wave Freq. (f_2)
F_x	±4.6%	±0.4%	±1.2%
F_z	±14%	±0.6%	±1.6%
M_y	±1.8%	±0.4%	±0.7%

Total Combined Uncertainty

Finally, the estimated combined uncertainties (approximately 95% confidence), expressed as percentages of the baseline solution in TABLE 6, are provided in TABLE 11. The total uncertainties in heave force are considerably higher than those in surge force and pitch moment at all three frequencies, reflecting the difficulty in accurately capturing the viscous excitation on the heave plate. At the difference frequency, the uncertainty in heave-force amplitude reached 47% while the more important surge force and pitch moment both have significantly lower uncertainties. This is a most fortuitous outcome because the difference-frequency heave force is of little engineering importance considering the high heave resonance frequency.

TABLE 11: TOTAL UNCERTAINTIES IN WAVE-LOAD AMPLITUDES FOR THE BASELINE SOLUTION

	Diff. Freq. (f_d)	1st Wave Freq. (f_1)	2nd Wave Freq. (f_2)
F_x	±26%	±3.9%	±6.0%
F_z	±46%	±11%	±13%
M_y	±17%	±7.6%	±3.0%

4.2.2 Correction to Difference-Frequency Forces and Moments

The contributions from the difference-frequency free waves to the second-order wave loads can be approximately removed since the free waves are linear:

$$\tilde{A}_{f,j}(f_d) = A_{f,j}(f_d) - \zeta_{if}X_j(f_d, \theta = 0) - \zeta_{rf}X_j(f_d, \theta = \pi) \quad (9)$$

where $\tilde{A}_{f,j}(f_d)$ and $A_{f,j}(f_d)$ are the corrected and uncorrected force/moment amplitude in the jth ($j = 1,2,...,6$) direction at the difference frequency f_d. The complex amplitudes of the incident and reflected free waves ζ_{if} and ζ_{rf} can be obtained from the unobstructed incident wave field using the wave-splitting method described in Section 4.1. Finally, X_j is the unit-amplitude wave-exciting force/moment in the jth direction that depends on the wave frequency and incident wave direction θ (the angle between wave direction and the x-axis). X_j can be obtained from linear potential-flow theory. Since the amplitudes of the free waves were quite small, any higher-order effects not considered in Eq. (9) should be negligible. The above correction procedure was found to be valid based on a limited preliminary study. A more comprehensive evaluation will be performed in the future.

The corrected and normalized amplitudes of difference-frequency wave loads obtained with the baseline configuration are given in TABLE 12. The corresponding values before the correction are also included for reference. Overall, the correction is significant for heave but relatively minor for surge and pitch.

TABLE 12: NORMALIZED AMPLITUDES OF DIFF.-FREQ. WAVE LOADS BEFORE AND AFTER CORRECTION

	Before Correction	After Correction
F_x	0.8408	0.7920
F_z	1.7662	2.7975
M_y	1.6815	1.6504

## 5. COMPARISON OF RESULTS FROM PARTICIPANTS AND POTENTIAL-FLOW PREDICTIONS

The CFD predictions of the wave loads from the various participants of the OC6 project are shown in FIGURES 10-12. The estimated total uncertainties from Section 4.2.1 are added to the results from NREL for reference. The difference-frequency wave loads from the participants have all been corrected with the procedure described in Section 4.2.2. The hatched bars indicate potential-flow predictions. For the two wave frequencies, the linear wave-exciting forces and moments are shown. For the difference frequency, the wave loads predicted by second-order potential-flow QTFs are used.

Overall, the surge force and pitch moment at the two wave frequencies were consistently predicted. Except for DTU, the variation across participants is generally small, consistent with the small uncertainty estimate. DTU results show very high surge-force and pitch-moment amplitudes at the first wave frequency. This was caused by significant wave reflection of the first wave component from the downstream boundary present in the DTU solutions. The CFD predictions for surge force and pitch moment are generally close to, but slightly higher than, those of the linear potential-flow theory for the majority of the

participants, indicating only minimal viscous excitation. In contrast, the CFD results for heave force at the lower wave frequency f_1 tend to be significantly higher than the potential-flow prediction, which suggests significant viscous excitation in heave on the large heave plates. The variation in CFD results for the heave force from the various participants is also more pronounced likely due to the difficulty in accurately resolving the effect of flow separation at the corners of the heave plates. This difficulty is also reflected by the higher uncertainty in NREL results.
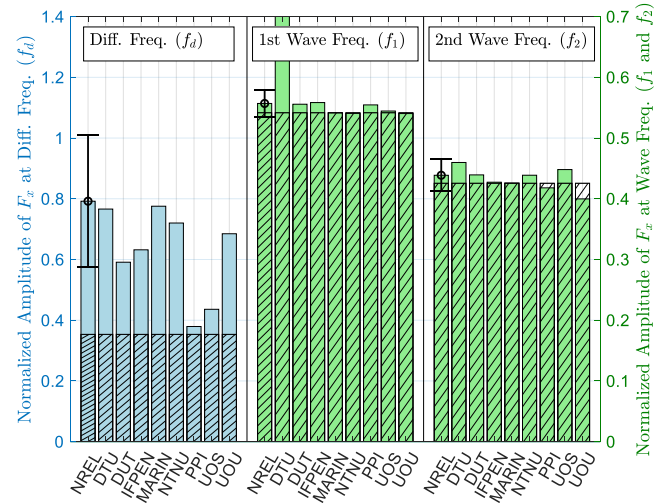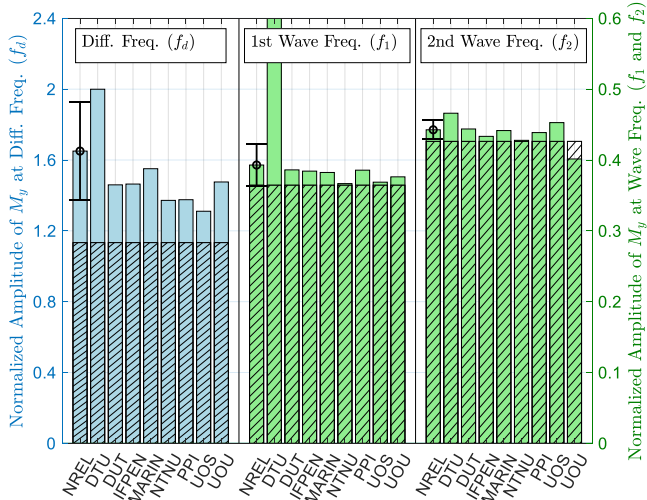

FIGURE 10: AMPLITUDES OF WAVE-INDUCED SURGE FORCE (F_x) ON THE PLATFORM AT THE DIFF. FREQ. (f_d) AND WAVE FREQUENCIES (f_1 AND f_2).
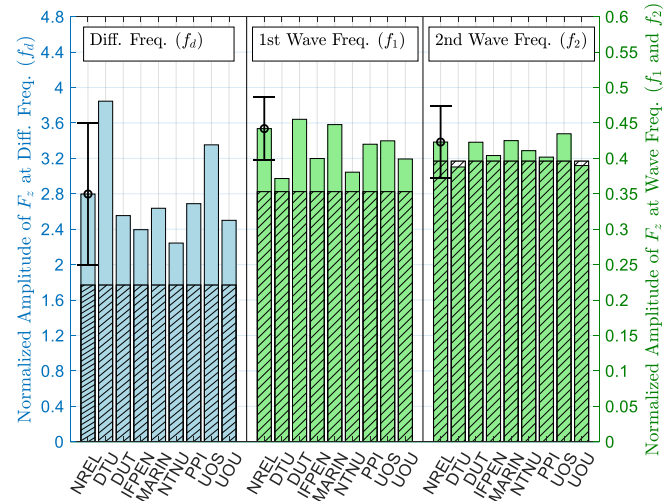
FIGURE 11: AMPLITUDES OF WAVE-INDUCED HEAVE FORCE (F_z) ON THE PLATFORM AT THE DIFF. FREQ. (f_d) AND WAVE FREQUENCIES (f_1 AND f_2).

Due to the small (unnormalized) magnitude, accurately capturing the nonlinear difference-frequency loads can be much more challenging. Compared to the wave-frequency loads, the variation in the difference-frequency loads from the participants is generally more significant. Correspondingly, the uncertainty intervals for the NREL results are also higher. Nevertheless, the

results from a majority of the OC6 participants show a degree of consistency that is nontrivial for second-order nonlinear loads, especially considering the differences among the numerical set-ups adopted by the participants. In fact, most participant results lie within the uncertainty band around the NREL results with only a few exceptions. This observation suggests that it may be feasible to consistently predict the nonlinear difference-frequency wave loads on the platform using CFD.

FIGURE 12: AMPLITUDES OF WAVE-INDUCED PITCH MOMENT (M_y) ON THE PLATFORM AT THE DIFF. FREQ. (f_d) AND WAVE FREQUENCIES (f_1 AND f_2).

Furthermore, the difference-frequency loads predicted by potential-flow QTFs are, for the most part, below CFD predictions, even considering the uncertainties in the CFD results. It may, therefore, be beneficial to calibrate the engineering models of offshore wind platforms, which were found to frequently underpredict low-frequency loads and responses [5], using the CFD results for a collection of strategically selected bichromatic-wave cases.

6. CONCLUSIONS
As part of Phase I of the OC6 project, the feasibility of estimating nonlinear low-frequency wave loads on a semisubmersible offshore wind platform using CFD was investigated collaboratively. A fixed platform in bichromatic incident waves was simulated. The use of bichromatic waves with a short repeat period, instead of irregular waves, shortens the physical time that needs to be simulated, significantly reducing the computing time. The resulting difference-frequency load can also be directly compared to the quadratic transfer functions from 2nd order potential-flow theory.

A numerical convergence study and a systematic evaluation of uncertainty was performed for the CFD results from NREL. Sources of uncertainty considered included numerical space and time discretization, effect of finite domain size, and processing uncertainty due to the fluctuation of force/moment amplitudes over the analysis range. CFD predictions of surge-force and pitch-moment amplitudes at the two wave frequencies were found to have relatively low uncertainty, and the CFD results

were close to those of linear potential flow theory, indicating minimal viscous effects on those force components. Higher uncertainty was estimated for the wave-frequency heave force which also showed significant contribution from viscous excitation. The higher uncertainty in heave force reflects the difficulty in accurately capturing the effect of flow separation from the heave plates of the platform. Predicting the second-order difference-frequency wave loads is considerably more challenging due to their smaller magnitudes. The relative uncertainties in the difference-frequency loads were also correspondingly higher. Nevertheless, the CFD results from the participants were consistently higher than potential-flow QTFs even with uncertainties considered. Therefore, CFD results of a collection of strategically selected bichromatic-wave cases have the potential to be used to calibrate the engineering models of offshore wind platforms, which often suffers from the underprediction of nonlinear low-frequency wave loads and platform responses.

The CFD results from the participants of the OC6 project were also compared to each other. Interestingly, the variation among the participant results was largely consistent with the estimated uncertainty. As expected, the relative variation in difference-frequency loads was more significant; however, most participant results agreed with the results from NREL to within the estimated numerical uncertainty. This level of agreement is nontrivial considering the difference among the numerical set-ups adopted by the participants. This observation suggests that CFD can provide consistent estimates of the nonlinear low-frequency wave loads on a semisubmersible offshore wind platform. Of course, validation of those results can only be achieved when comparison with wave-basin experiments is done. An experimental validation campaign designed for this purpose is planned for the near future.

REFERENCES

[1] Simos, A. N., Sparano, J. V., Aranha, J. A. P., and Matos, V. L. F., "2nd order hydrodynamic effects on resonant heave, pitch and roll motions of a large-volume semi-submersible platform." *Proceedings of the ASME 27th International Conference on Offshore Mechanics and Arctic Engineering*, pp. 229-237, 2008.

[2] Bayati, I., Jonkman, J., Robertson, A., and Platt, A., "The effects of second-order hydrodynamics on a semisubmersible floating offshore wind turbine." *Journal of Physics: Conference Series*, Vol. 524, p. 012094, 2014.

[3] Robertson, A., et al., "OC5 Project Phase II: Validation of global loads of the DeepCwind floating semisubmersible wind turbine." *Energy Procedia*, Vol. 137, pp. 38-57, 2017.

[4] Simos, A. N., Ruggeri, F., Watai, R. A., Souto-Iglesias, A., and Lopez-Pavon, C., "Slow-drift of a floating wind turbine: An assessment of frequency-domain methods based on model tests." *Renewable Energy*, Vol. 116, pp. 133-154, 2018.

[5] Robertson, A., et al., "OC6 Phase I: Investigating the under-prediction of low-frequency hydrodynamic loads and responses of a floating wind turbine." *Proceedings of the EAWE's TORQUE 2020 Conference,* 2020. [under review].

[6] U.S. Department of Energy (DOE), OC6 - Offshore Code Comparison Collaboration, Continued, with Correlation and unCertainty, https://a2e.energy.gov/projects/oc6

[7] Tom, N., Robertson, A., Jonkman, J., and Wendt, F., "Bichromatic wave selection for validation of the difference-frequency transfer function for the OC6 validation campaign." *Proceedings of the 2nd International Offshore Wind Technical Conference*, pp. V001T01A022, 2019.

[8] Shao, Y.-L. and Faltinsen, O. M., "A numerical study of the second-order wave excitation of ship springing by a higher-order boundary element method." *International Journal of Naval Architecture and Ocean Engineering*, Vol. 6**,** No. 4, pp. 1000-1013, 2014.

[9] Siemens PLM Software, *Simcenter STAR-CCM+ User Guide*, Version 13.06.012. 2018.

[10] OpenCFD Ltd., *OpenFOAM, The Open Source CFD Toolbox User Guide*, Version v1812. 2018.

[11] Jacobsen, N. G., *waves2Foam Manual*, Version 0.9 (Draft). 2017.

[12] IH Cantabria, *IHFOAM Manual*. 2014.

[13] Larsen, B. E. and Fuhrman, D. R., "On the over-production of turbulence beneath surface waves in Reynolds-averaged Navier-Stokes models." *Journal of Fluid Mechanics*, Vol. 853, pp. 419-460, 2018.

[14] Higuera, P., Lara, J. L., and Losada, I. J., "Realistic wave generation and active wave absorption for Navier-Stokes models: Application to OpenFOAM®." *Costal Engineering*, Vol. 71, pp. 102-118, 2013.

[15] NUMECA International, *HEXPRESS, Unstructured Full-Hexahedral Meshing*. 2019.

[16] ReFRESCO, *ReFRESCO v2.6.0 Documentation*. 2020

[17] OpenCFD Ltd., *OpenFOAM, The Open Source CFD Toolbox User Guide*, Version v1712. 2017.

[18] OpenFOAM Foundation, *OpenFOAM v4 User Guide*. 2016.

[19] ANSYS Inc., *ANSYS Fluent 19.2 User Guide*. 2018.

[20] Waals, O. J., "On the application of advanced wave analysis in shallow water model testing (wave splitting)." *Proceedings of the ASME 28th International Conference on Ocean, Offshore and Arctic Engineering*, pp. 415-423, 2009.

[21] Ogilvie, T. F., "Second-order hydrodynamic effects on ocean platforms." *Proceedings of the International Workshop on Ship and Platform Motions*, pp. 205-265, 1983.

[22] Eça, L., "On the influence of the iterative error in the numerical uncertainty of ship viscous flow calculations." *Proceedings of the 26th Symposium on Naval Hydrodynamics*, 2006.

[23] Eça, L. and Hoekstra, M., "A procedure for the estimation of the numerical uncertainty of CFD calculations based on grid refinement studies." *Journal of Computational Physics*, Vol. 262, pp. 104-130, 2014.

[24] Eça, L. and Hoekstra, M., "Evaluation of numerical error estimation based on grid refinement studies with the method of the manufactured solutions." *Computers & Fluids*, Vol. 38, pp. 1580-1591, 2009